ACES Asian Chemical Editorial Society

doi.org/10.1002/cnma.202500248

CHEMNANOMAT
Research Article

www.chemnanomat.org

Mechanochemical Synthesis of Highly Disordered Transition Metal Dichalcogenide Nano Catalysts for Hydrogen Evolution Reaction

Suleyman Can and Cihan Kuru*

Although transition metal dichalcogenide (TMD) catalysts have been widely studied, their large-scale production remains a challenge. In this study, a readily scalable and ubiquitous mechanochemical synthesis method, for the production of TMD nano catalysts, is developed. For the first time, the direct mechanochemical synthesis of MoS_2 and $MoSe_2$ nano catalysts from easily accessible elemental precursors (Mo, S and Se) is demonstrated. About 2 g of MoS_2 and $MoSe_2$ nano powder could be produced in a single batch with a yield of 94.3% and 90.9%, respectively. The synthesized catalysts are in the form of nanosheets whose thickness range from 5 to 10 layers and have a highly disordered structure that is coveted for catalysis applications. The MoS_2 and $MoSe_2$ nanosheets exhibit an excellent catalytic activity in hydrogen evolution reaction with an overpotential of 275 and 211 mV to deliver 100 mA cm^{-2} current density and a Tafel slope of 75 and 48 mV dec^{-1}, respectively. Nearly amorphous structure of the nanosheets incorporating point defects and sulfur/selenium vacancies is the main contributing factor to the high catalytic activity. The proposed method can be implemented to the synthesis of other nano TMDs, fueling future research activity.

1. Introduction

The excessive use of fossil fuels since the onset of the industrial revolution has increased the CO_2 level in the atmosphere dramatically, raising concerns about climate change and human health.[1] To mitigate the adverse effects of the climate change, European Union set a goal to become climate neutral by 2050, which requires the complete abandonment of the fossil fuels.[2] Among alternatives, green hydrogen is quite advantageous owing to its zero carbon emission, high energy efficiency and versatility to be used in residential buildings, industrial plants, and transportation.[3] The primary concerns regarding the widespread use of hydrogen stem from production and storage. Research has focused on metal hydrides[4–9] for hydrogen storage whereas electrolysis powered by renewable energy is the most plausible method for green hydrogen production.[10,11] However, the process of converting renewable energy to hydrogen is not efficient mainly due to intrinsically low efficiencies of the solar cells and wind turbines.[12] In addition to that, there are electrochemical losses in the electrolysis cell that are related to electrode polarization, ion transport and cell resistance.[13] As a result, the voltage required for the electrolysis of water is higher than the theoretical decomposition voltage of water. This is referred as overpotential and it can be minimized using appropriate catalyst materials.[14] Pt is known as the best catalyst for hydrogen evolution reaction (HER) with an overpotential close to zero.[15] Despite its excellent catalytic activity, the large-scale implementation of Pt is hindered by its high cost and limited reserves.[16,17] Hence, it is essential to develop low cost and durable catalysts that have a comparable catalytic activity to Pt.

Recently, transition metal dichalcogenide (TMDs) have become promising candidates to replace Pt-based catalysts in HER.[18–20] TMDs exhibit high catalytic activity due to the near-zero ΔG_{H^*} of the edge sites.[21,22] However, low electrical conductivity and the catalytically inert nature of the basal plane of the TMDs limit their HER performance.[23–26] Substantial research efforts have been devoted to the fabrication of the nanostructured TMDs with rich edge regions to improve the catalytic activity. TMD catalysts in the form of nanoparticles,[27,28] nanowires,[29,30] and nanorods[31,32] have been demonstrated as active catalysts in HER. In addition, studies have been carried out to reduce the nanosheet size and produce porous nanosheets to enrich the edge regions.[33,34] Moreover, 1 T phase MoS_2 and $MoSe_2$ nanosheets prepared by lithium intercalation and hydrothermal methods have been demonstrated to exhibit metallic conductivity and possess active sites on their basal plane, resulting in significantly higher catalytic activity compared to their 2 H phase counterparts.[35] Furthermore, the design of TMD-graphene/carbon nanotube-based hybrid electrodes has led to superior HER activity due to the increased surface area and enhanced electrical conductivity.[36,37] Another strategy to enhance the HER activity of the TMDs is to activate the basal surface through creating defects and sulfur/selenium vacancies.[38,39] Besides, it has been reported that amorphous MoS_x films exhibit very high activity due to the presence of a significant number of active sites in their structure.[40,41] These studies reveal that the HER activity of the TMD catalysts can be significantly enhanced through shape and size control, phase engineering, the design of TMD-carbon-based hybrid electrodes, defect and vacancy modification and the formation of amorphous structures.

S. Can, C. Kuru
Department of Metallurgical and Materials Engineering
Bilecik Seyh Edebali University
Bilecik 11100, Turkey
E-mail: cihan.kuru@bilecik.edu.tr

Supporting information for this article is available on the WWW under https://doi.org/10.1002/cnma.202500248

TMDs can be prepared by bottom-up and top-down approaches including chemical vapor deposition,[42] hydrothermal synthesis,[43] wet chemical synthesis,[44] ultrasonic delamination,[45] lithium intercalation[46] and electrochemical exfoliation.[47] Additionally, mechanochemical synthesis method may offer a new approach to the TMDs synthesis. In the mechanochemical synthesis, the precursors usually in dry state undergo a chemical reaction through the exertion of forces induced by the repetitive collisions of the milling balls.[48] The mechanochemical synthesis has several significant advantages over the other production methods, namely allowing reactions to occur at room temperature, eliminating the need for organic solvents, simplicity of process parameters and high production capacity due to its scalability.[49] Previously, mechanochemical synthesis of metal dichalcogenide nanoparticles such as CdS, Ce_2S_3 and ZnS has been accomplished by the reaction of metal chloride (MCl_x) salts with CaS or Na_2S.[50] In addition, MoS_2 has been synthesized by a two-step method comprised of wet chemical reaction of $(NH_4)_2MoO_4$ with Na_2S to form amorphous MoS_3 and subsequent mechanochemical reduction to MoS_2.[51] Furthermore, ball milling has been shown as an effective way to prepare exfoliated MoS_2 nanosheets.[52,53] However, direct mechanochemical synthesis of TMDs such as MoS_2 or $MoSe_2$ has not been reported.

In the present work, highly disordered MoS_2 and $MoSe_2$ nanosheets have been synthesized by the mechanochemical reactions of elemental Mo, S and Se under Ar atmosphere. The synthesis parameters of ball to powder ratio (BPR), milling time and the molar ratio of the solid dispersant to the reactants were optimized to attain maximum MoS_2 and $MoSe_2$ yield. The structural and chemical properties of the MoS_2 and $MoSe_2$ were determined by X-ray diffraction (XRD), Raman spectroscopy, photoluminescence (PL) spectroscopy, X-ray photoelectron spectroscopy (XPS), transmission electron microscopy (TEM), scanning electron microscopy (SEM), energy dispersive X-ray (EDX), Brunauer–Emmett–Teller (BET) and Barrett–Joyner–Halenda (BJH) analysis. The catalytic performance of the MoS_2 and $MoSe_2$ in HER was determined in acidic solution by electrochemical measurements.

2. Results and Discussion

The synthesis of the MoS_2 and $MoSe_2$ catalysts were carried out by solid-state mechanochemical reactions of elemental Mo, S and Mo, Se powders with a stoichiometric ratio of 1:2 (**Scheme 1**). The synthesis parameters were optimized by studying the effect of BPR, milling time and the amount of NaCl solid dispersant on the product yield. **Figure 1**a shows the XRD patterns of the products obtained by the mechanochemical reaction of Mo and S powders under the BPR of 10:1, 50:1 and 100:1. No XRD peaks related to MoS_2 phases could be detected for the BPR of 10:1 and 50:1 while increasing the BPR to 100:1 resulted in appearance of a new peak at 14.12°, indicating the formation of MoS_2. Increasing the BRP facilitates the formation of MoS_2 by increasing the frequency of the collisions between the balls and the reactants and providing higher impact energy. However, the BPR ratio was limited to 100:1 because larger BPR values pose a high risk of contamination due to self-milling of the stainless steel balls. The

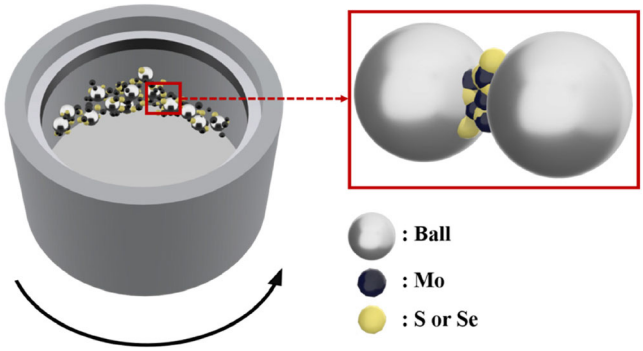

Scheme 1. Schematic of the mechanochemical synthesis of the TMD nano catalysts.

effect of milling time was investigated by conducting the mechanochemical synthesis of MoS_2 under a BPR of 100:1 for 24, 48 and 72 h. As the milling time is increased, the intensity of the MoS_2 peak at around 14.12° grows substantially (Figure 1b). Nevertheless, an intense Mo peak at 40.56° can be still detected even after 72 h of milling, implying that there is still a large amount of unreacted Mo left in the product. To further optimize the process, NaCl powder was added into the reactor as a solid dispersant. Solid dispersants prevent the cold welding and agglomeration of the particles by imposing a physical barrier.[48] We found that NaCl solid dispersant also promotes the reaction of Mo and S since equimolar amount of NaCl led to a dramatic increase in the intensity of the MoS_2 peak while diminishing the Mo peak (Figure 1c). Yet, MoS_2 yield drops when increasing the NaCl molar ratio to 3:1 as excess volume of NaCl powder slows down the reaction. Therefore, the optimum conditions for the mechanochemical synthesis of MoS_2 are 100:1 BPR, 72 h milling time and 1:1 NaCl:(Mo+S) molar ratio. The same experimental conditions were adopted for the synthesis of the $MoSe_2$. Figure 1d displays the XRD patterns of the MoS_2 and $MoSe_2$ catalysts synthesized under the optimized conditions. The diffraction peaks of the MoS_2 sample at 14.12°, 32.9° and 58.8° match with the (002), (100) and (110) reflections of hexagonal MoS_2 crystal structure (JCPDS # 01-075-1539). On the contrary, $MoSe_2$ sample exhibits peaks at 13.52°, 31.28°, 32.40°, 34.78°, 47.52°, 53.74°, 57.16° and 65.76°, which coincide with the (002), (100), (101), (102), (105), (106), (008) and (200) planes of hexagonal $MoSe_2$ phase (JCPDS # 01-087-2419). In addition, the samples display a peak at around 26.06° arising from MoO_2 (JCPDS # 01-086-0135) and two peaks at around 40.56° and 73.68° corresponding to Mo (JCPDS # 00-001-1207). The intensities of the Mo peaks are relatively small for both samples, indicating that most Mo was converted to MoS_2. The Rietveld refinement was applied on the XRD data to determine the percentage of the each phase in the products (Figure S1, Supporting Information). The calculated amount of the MoS_2 and $MoSe_2$ phases are 94.3 and 90.9 % while the samples contain 0.8% and 2% Mo and 4.9 and 7.1% MoO_2, respectively.

BET and BJH analysis were performed to measure the specific surface area and average pore width of the catalyst samples. N_2 adsorption isotherms (Figure S2a and c, Supporting Information) revealed a specific surface area of 9.76 and 31.01 $m^2 g^{-1}$ for the

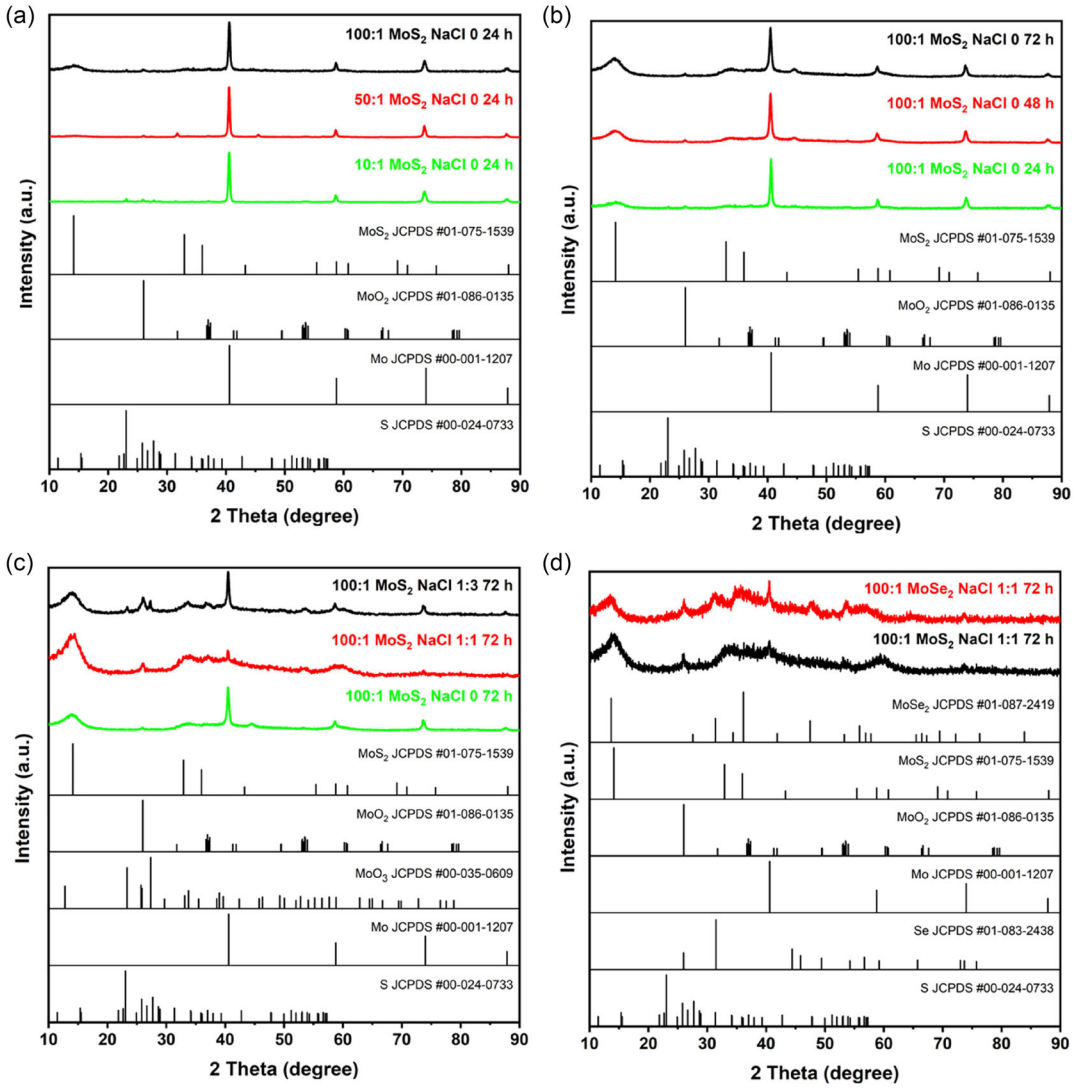

Figure 1. The XRD patterns of the products obtained from the mechanochemical synthesis of Mo and S under varying a) BRP, b) milling time and c) NaCl ratio. d) The XRD patterns of the MoS_2 and $MoSe_2$ catalysts under the optimized conditions.

MoS_2 and $MoSe_2$ nano catalysts, respectively. The larger specific area of the $MoSe_2$ nano catalysts indicates a lesser degree of agglomeration due to cold welding during the mechanochemical synthesis. BJH adsorption differential pore volume plots indicate that both samples predominantly have a mesoporous structure with an average pore width of 12.3 and 11.9 nm (Figure S2b and d, Supporting Information). The relatively large pore size of the samples facilitates the diffusion of electrolyte, improving the HER performance.

TEM measurements were conducted to investigate the morphological properties and crystal structure of the synthesized TMDs. Both MoS_2 and $MoSe_2$ are in the form of nanosheets (**Figure 2**a and **Figure 3**a). Some individual nanosheets whose lateral dimensions are on the order of a few tens of nanometers as well as micrometer size agglomerates were observed under the TEM microscope. The high-resolution TEM images show the co-existence of crystalline (encircled in red) and highly disordered regions in the nanosheets (Figure 2b and Figure 3b). The measured interplanar distance marked in yellow in Figure 2b and Figure 3b are 0.66 and 0. 70 nm, which correspond to (002) planes of the MoS_2 and $MoSe_2$ phases, respectively. The slightly larger interlayer spacing of the nanosheets compared to the values reported in the literature (0.62 nm and 0.67 nm)[54,55] indicates a layer expansion. The number of the lattice fringes of vertically aligned nanosheets indicates that the nanosheets are 5 to 10 layers thick. The close up images of the crystalline regions presented in Figure 2c and Figure 3c exhibit an interplanar distance of 0.25 and 0.26 nm, coinciding with the (102) planes of MoS_2 and $MoSe_2$, respectively.[56,57] In addition, the black voids in the lattice fringes point out the presence of point defects in the crystalline regions. The co-existence of the crystalline and amorphous regions in the MoS_2 and $MoSe_2$ nanosheets was verified by the selected-area electron diffraction (SAED) patterns, which consist of concentric dot circles and diffusive rings (Figure 2d and Figure 3d). The concentric dot circles correspond to the small crystalline grains observed in the TEM images while the diffusive rings indicate an amorphous structure.[58,59] The SAED pattern of the MoS_2 sample can be indexed to (004), (100), (103), (105), (110) and (116) planes of 2 H-MoS_2 (JCPDS # 01-075-1539) whereas the

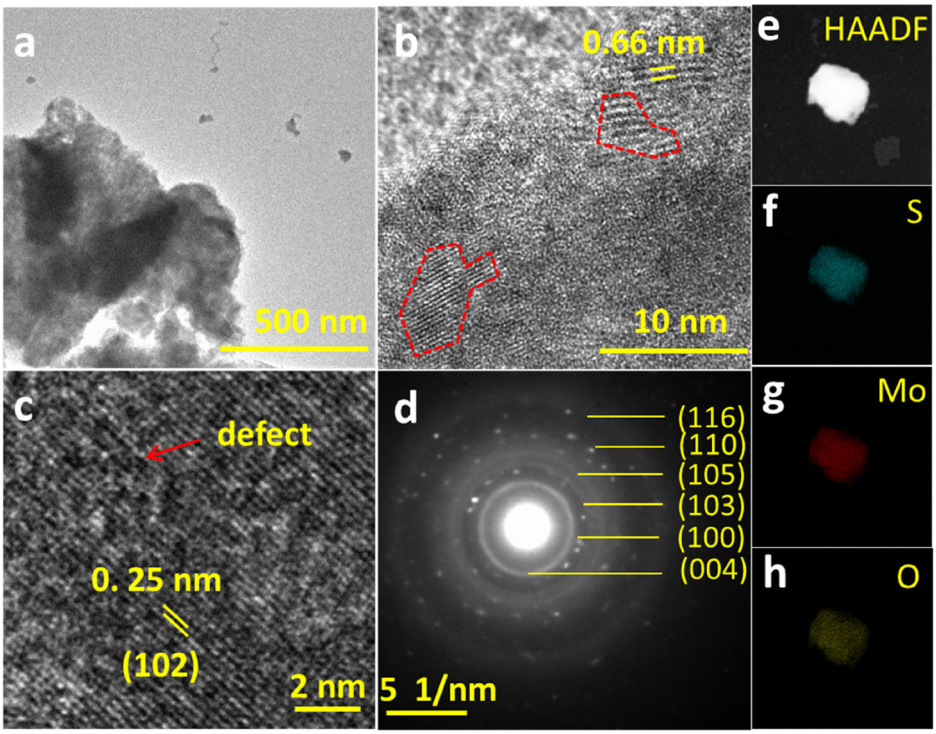

Figure 2. a) Low and b) high-resolution TEM images of the MoS_2 nanosheets. c) Close-up image of a crystalline region oriented in (102) direction. d) SAED pattern and e) HAADF image of a cluster of MoS_2 nanosheets. EDX mapping images of the f) S, g) Mo and h) O elements.

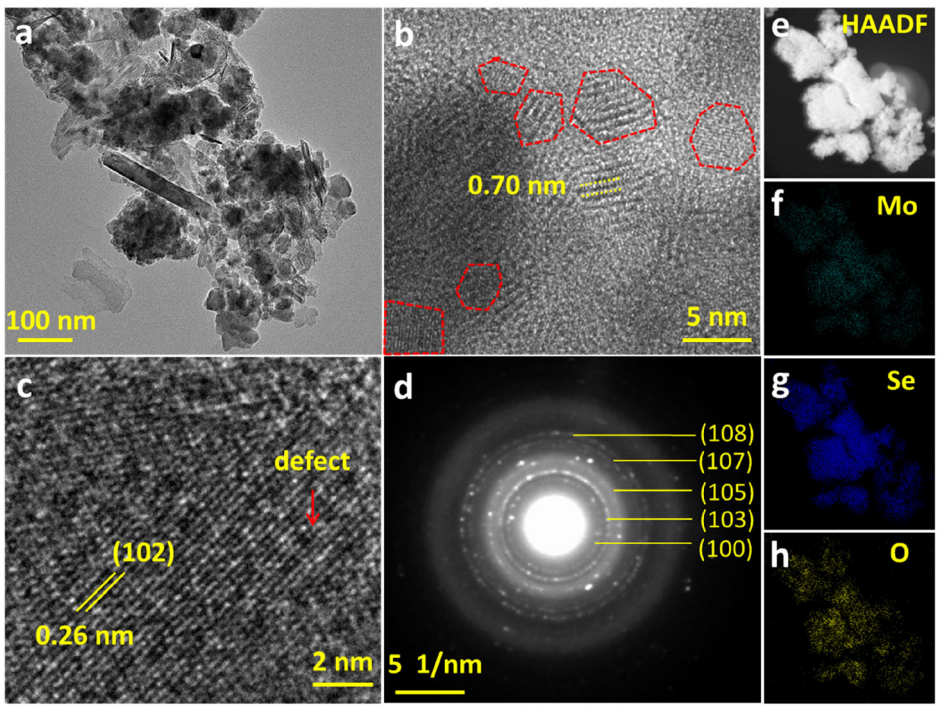

Figure 3. a) Low and b) high-resolution TEM images of the $MoSe_2$ nanosheets. c) Close-up image of a crystalline region oriented in (102) direction. d) SAED pattern and e) HAADF image of a cluster of $MoSe_2$ nanosheets. EDX mapping images of the f) Mo, g) Se and h) O elements.

$MoSe_2$ sample exhibits 100, 103, 105, 107 and 108 reflections of 2 H-$MoSe_2$ (JCPDS # 01-087-2419), which are both consistent with the XRD measurements. Moreover, EDX mapping results indicate the presence of S, Mo and O (Figure 2e,f,g,h) elements in the MoS_2 and Mo, Se and O (Figure 3e,f,g and h) elements in the $MoSe_2$ samples.

XPS measurements were performed to analyze the surface chemical composition and chemical bonds of the MoS_2 and

$MoSe_2$ nano catalysts. **Figure 4**a,b show the XPS survey scans of the MoS_2 and $MoSe_2$, in which peaks originating from Mo, S, Se, C and O elements could be detected. The absence of Fe peaks indicates that no contamination occurred from the stainless steel milling jar or the balls. The high-resolution XPS scan of Mo 3 d for the MoS_2 catalyst is displayed in Figure 4c, where the spectrum can be deconvoluted into two different doublets. The Mo^{+4} $3d_{5/2}$ and Mo^{+4} $3d_{3/2}$ doublet centered at 229.7 and 232.8 eV arises from Mo—S bonds of the MoS_2 whereas the Mo^{+6} $3d_{5/2}$ (232.9 eV) and Mo^{+6} $3d_{3/2}$ (236.0 eV) doublet implies the formation of MoO_3 compound.[60,61] Moreover, the peak at 227.0 eV corresponds to S 2s orbital.[60] The Mo^{+4} $3d_{5/2}$ (229.5 eV), Mo^{+4} $3d_{3/2}$ (232.6 eV), Mo^{+6} $3d_{5/2}$ (232.8 eV) and Mo^{+6} $3d_{3/2}$ (235.9 eV) signals could also be detected for the $MoSe_2$ catalyst (Figure 4d), indicating the co-presence of the $MoSe_2$ and MoO_3 phases. As the MoO_3 phase could be only detectable by the XPS measurements, we can conclude that the formation of the MoO_3 only occurs on the surface of the catalysts most likely due to contact with air. The fraction of the MoO_3 phase was calculated by peak integration, yielding a value of 66% and 30% for the MoS_2 and $MoSe_2$ catalysts, respectively. This result shows that the MoS_2 surface is more heavily oxidized compared to $MoSe_2$. No peaks related to Mo^0 3 d could be detected, confirming that the great majority of the Mo converted to MoS_2 and $MoSe_2$. In the S 2p region of the MoS_2 (Figure 4e), two peaks located at 162.6 and 163.8 eV can be attributed to the S^{-2} $2p_{3/2}$ and S^{-2} $2p_{1/2}$ whereas the doublet

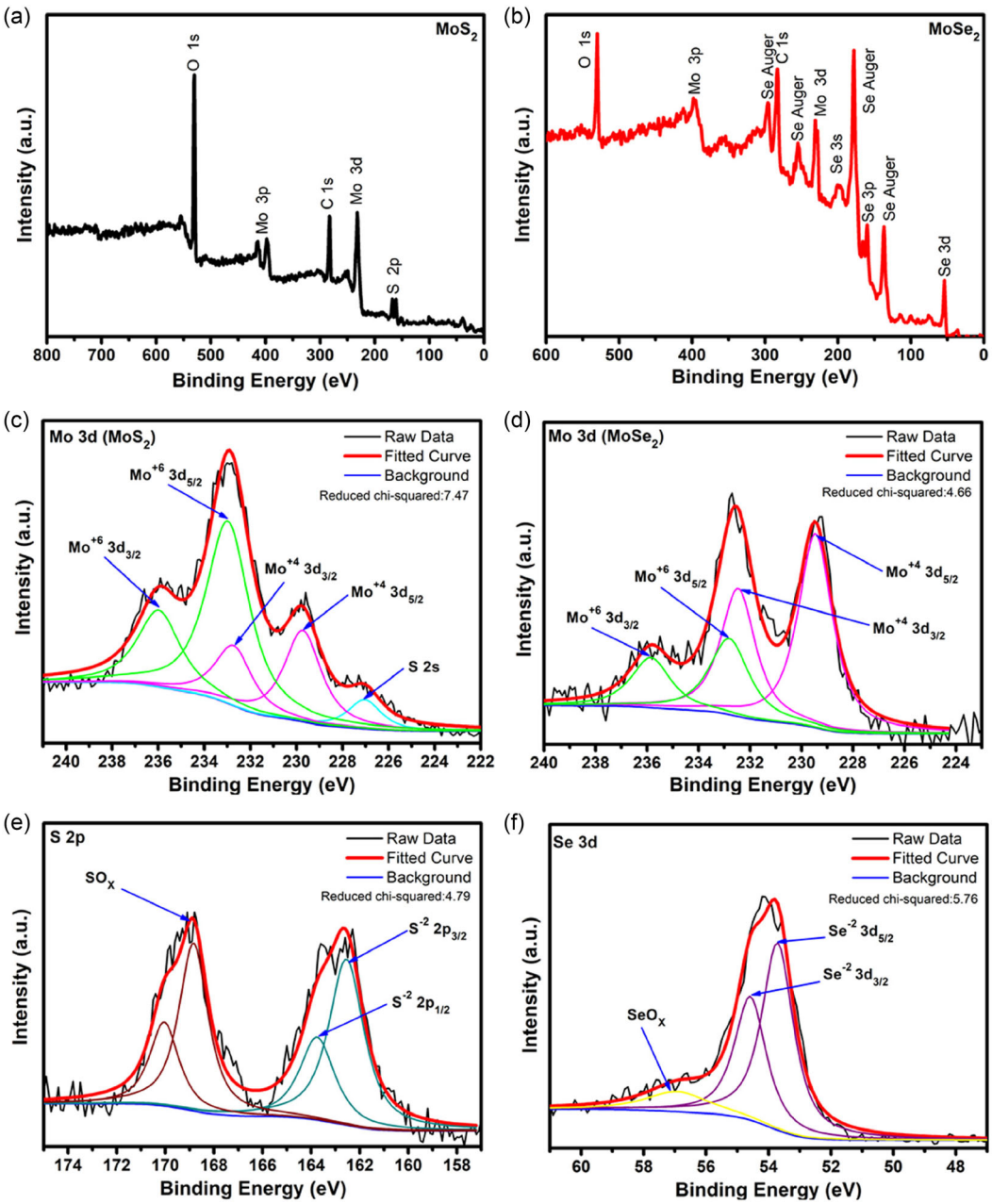

Figure 4. Survey scan XPS spectra of the a) MoS_2 and b) $MoSe_2$ nanosheets. High- resolution Mo 3d XPS spectra of the c) MoS_2 and d) $MoSe_2$ nanosheets. e) S 2p and f) Se 3d XPS spectra of the MoS_2 and $MoSe_2$ samples, respectively.

appearing at higher binding energies results from the S—O bonds.[62] On the contrary, Se 3d spectrum of the $MoSe_2$ (Figure 4f) exhibits peaks at 53.7 and 54.6 eV, corresponding to Se^{-2} $3d_{5/2}$ and Se^{-2} $3d_{3/2}$ doublets.[63] The additional small peak located at 56.9 eV indicates the partial oxidation of the Se atoms.[64] The S:Mo (1.48) and Se:Mo (1.75) atomic ratios have been calculated from the peak areas of the Mo 3d, S 2p and Se 3 d spectra. The S:Mo and Se:Mo ratios are lower than the stoichiometric ratio of 2, suggesting the existence of sulfur and selenium vacancies. The sulfur/selenium vacancies are prone to oxidation in ambient air due to their high chemical reactivity.[65] The Mo—O_3, S—O and Se—O bonds observed in the XPS data is resulted from the interaction of oxygen with the sulfur/selenium vacancies when the samples were exposed to ambient air.

Figure 5a shows the Raman spectra of the MoS_2 and $MoSe_2$ nanosheets. The characteristic peaks of the MoS_2 and $MoSe_2$ lay in the range of 100–500 cm^{-1}.[66,67] Both samples didn't exhibit vibrational modes in that region due to their highly disordered structure. PL spectra of the MoS_2 and $MoSe_2$ nanosheets are shown in Figure 5b, in which no emission peaks originating from the MoS_2 or $MoSe_2$ could be detected. The peak at 650 nm is due to the second order Rayleigh scattering of the source radiation (325 nm).[68] The nearly amorphous state of the nanosheets results in non-radiative recombination of the photo-generated carriers leading to flat PL spectra.

The HER activity of the mechanochemically synthesized MoS_2 and $MoSe_2$ nano catalysts were measured in a three-electrode configuration. The catalysts were loaded on a graphite rod after mixing with carbon black and Nafion, which ensured the electrical conductivity and robustness of the electrode. The HER data was fully iR compensated based on the series resistance (R_s) obtained from impedance measurements (Figure S3, Supporting Information). The R_s is the sum of the resistance of the cable connectors, graphite rod, catalyst and electrolyte. The R_s values of the catalysts loaded electrodes are comparable to bare graphite rod, indicating that the resistance contribution of the catalyst is negligible. Therefore, we can safely conclude that the data was not overcompensated and exaggerated. **Figure 6**a compares the polarization curves of the MoS_2, $MoSe_2$, Pt and carbon black. Both MoS_2 and $MoSe_2$ exhibit excellent HER performance with high current densities (j) at low overpotentials (η). The η to attain j of 10 and 100 mA cm^{-2} are 191 and 275 mV for the MoS_2 and 165 and 211 mV for the $MoSe_2$ catalysts, while Pt requires 23 and 75 mV to reach the same j values. In contrast, carbon black showed only a negligible HER activity over the measurement range. The HER mechanism of a catalyst can be evaluated based on the Tafel slope value obtained from the linear portion of a log (j) vs. η plot. The expected Tafel slopes are 120, 40 and 30 mV dec^{-1} when the rate-determining step is Volmer (adsorption), Heyrovsky (electrochemical desorption) or Tafel reaction (chemical desorption), respectively.[69] The yielded Tafel slope values for the MoS_2 (75 mV dec^{-1}) and $MoSe_2$ (48 mV dec^{-1}) implies Volmer–Heyrovsky mechanism whereas HER on Pt (36 mV dec^{-1}) follows the Volmer–Tafel reactions (Figure 6b, Figure S4, Supporting Information). The reported Tafel slope of pristine 2 H-MoS_2 and 2 H-$MoSe_2$ are on the order of 120 mV dec^{-1} indicating a rate-determining step of hydrogen adsorption.[70,71] Ideally, ΔG_{H^*} should be close to zero for HER catalysts.[72] The adsorption of hydrogen ions on the basal plane of the pristine 2 H-MoS_2 and 2 H-$MoSe_2$ is hindered due to their large positive ΔG_{H^*} values, resulting in sluggish HER kinetics.[73] The smaller Tafel slope of the mechanochemically synthesized MoS_2 and $MoSe_2$ suggests faster HER kinetics with a transition of the rate-determining step to hydrogen desorption. The mechanochemically synthesized MoS_2 and $MoSe_2$ have a highly disordered structure with point defects and sulfur/selenium vacancies. Amorphous MoS_2 has been shown as an active HER catalyst due to short Mo-Mo bonds, which results in a favorable ΔG_{H^*} value.[74] On the contrary, different types of defects including single sulfur/selenium vacancies have been proved to enhance the HER activity of TMDs by modulating the localized electron distribution of the surface atoms.[60,75,76] The sulfur/selenium vacancies increase the delocalized electron density nearby Mo atoms, promoting the adsorption of hydrogen ions and in turn enhancing the catalytic activity.[77] Such delocalized electrons also improve the electrical conductivity, further contributing to the enhanced catalytic activity. Hence, we can speculate that the combinative effects of the disordered structure, defects and sulfur/selenium vacancies play a crucial role in the observed high activity of the mechanochemically synthesized MoS_2 and $MoSe_2$, resulting

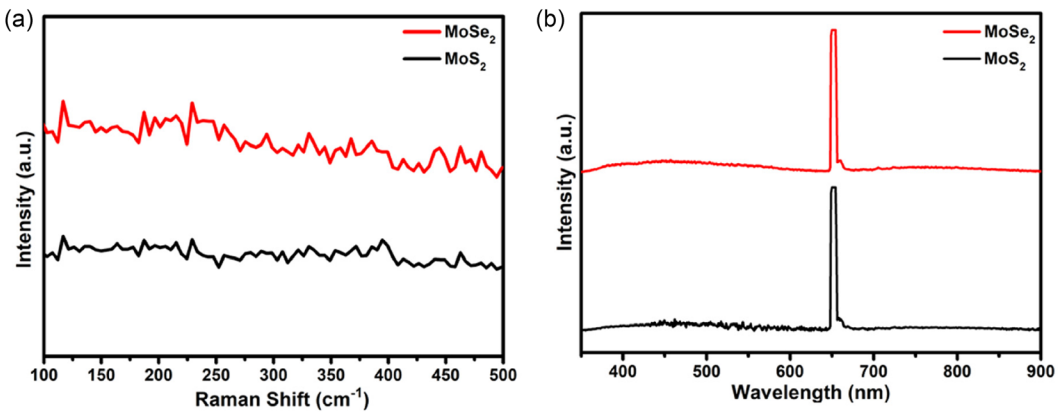

Figure 5. a) Raman and b) PL spectra of the MoS_2 and $MoSe_2$ nanosheets.

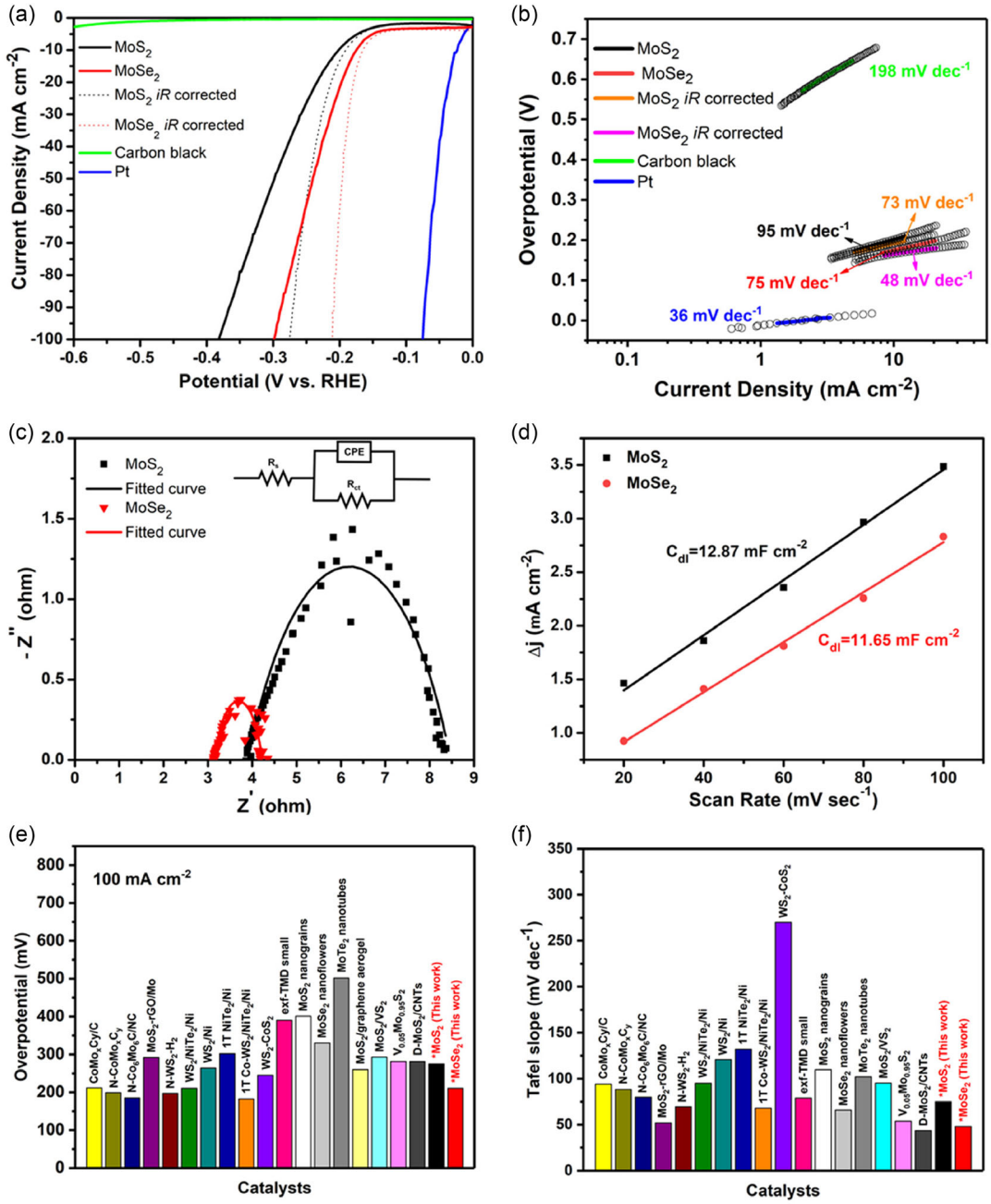

Figure 6. a) LSV curves and b) Tafel plots of the catalysts tested in HER. c) Nyquist plots and d) Δj–scan rate plots of the MoS_2 and $MoSe_2$ catalyst samples. e) Overpotential and f) Tafel slope comparison bar charts of various TMD catalysts reported in literature including this work.

in an ideal ΔG_{H^*} value and facilitated hydrogen adsorption. Exchange current density (j_o) is another parameter to assess the activity of a catalyst material. j_o is defined as the current density at the thermodynamic equilibrium potential and can be determined from the extrapolation of the linear portion of the log (j) versus η plot to zero η.[78] The obtained j_o for the MoS_2 and $MoSe_2$ are 20 μA cm^{-2} and 2.57 μA cm^{-2}, which are two-three orders of magnitude lower than Pt (2.39 mA cm^{-2}). Nonetheless, the mechanochemically synthesized MoS_2 and $MoSe_2$ catalysts stand in a good position when compared to other TMDs (Figure 6e,f) reported in the literature,[41,60,79–91] owing to high exchange current density, low overpotential and Tafel slope. Nyquist plots were constructed to evaluate the charge transfer kinetics of the MoS_2 and $MoSe_2$ catalysts. The Nyquist plots are shown in Figure 6c, in which both plots have a semicircle shape that can be well fitted into a modified Randle's model to extract charge transfer resistance (R_{ct}). $MoSe_2$ (1.1 Ω) has a lower R_{ct} than MoS_2 (4.5 Ω) at 250 mV η, which reflects its more efficient electron transfer ability at the electrolyte interface and better electrical conductivity. This is also corroborated by the lower R_s contribution of the $MoSe_2$ (0.1 Ω) on the graphite electrode compared to MoS_2 (0.8 Ω). Electrochemical surface area (ECSA) is an important factor that affects the HER performance of the catalysts. ECSA is proportional to C_{dl}[92] and therefore C_{dl}

can be used to evaluate the ECSA of the catalysts. C_{dl} is equal to half of the slope of the Δj-scan rate plots, where Δj represents the current density difference of the forward and backward CV scans (Figure S5, Supporting Information) taken in non-faradaic region. Both MoS_2 (12.87 mF cm^{-2}) and $MoSe_2$ (11.65 mF cm^{-2}) exhibits large C_{dl} (Figure 6d), indicating the abundance of accessible active sites, which is highly desirable for HER. Moderate oxidation of MoS_2 in which oxygen atoms are incorporated in the lattice has been reported to enhance the catalytic activity.[93,94] However, higher degree of oxidation is detrimental to HER because of the formation of MoO_3 compound, which has a lower conductivity than MoS_2 or $MoSe_2$. In our case, oxygen atoms are not incorporated into the MoS_2 or $MoSe_2$, rather they form MoO_3 species on the surface of the catalysts as indicated by the XPS results. The lower HER performance of the MoS_2 catalyst compared to $MoSe_2$ can be explained by its higher degree of oxidation, which is consistent with its larger R_s contribution.

We also studied the effect of using solid dispersant during the mechanochemical synthesis on the HER performance of the TMD catalysts. For this purpose, MoS_2 and $MoSe_2$ were synthesized under the same milling conditions except for the use of NaCl dispersant. Both catalysts show significantly lower HER performance compared to ones synthesized with NaCl (Figure S6a and b, Supporting Information). Moreover, they exhibit lower C_{dl} (Figure S6c and d, Supporting Information) and larger R_s (Figure S6e and f, Supporting Information) values as a result of their reduced ECSA and increased internal resistance due to the agglomeration and cold welding. This data clearly demonstrates the importance of the nano-size effect in catalysis.

The durability of the catalysts was assessed by recording the change in the current density over a period of 18 h (**Figure 7**a,b). The MoS_2 catalyst retained 71% of its initial current density after 18 h whereas the retention rate was 61% for the $MoSe_2$. To further investigate the stability of the samples, linear scan voltammetry (LSV) scans taken before and after the chronoamperometry test were compared (Figure 7c,d). Although there is a substantial decrease in the current density after 18 h, the LSV curves almost overlap, indicating the good stability of the MoS_2 and $MoSe_2$ nano catalysts. The performance degradation during the chronoamperometry test might be due to the clingy H_2 bubbles that reduce the effective surface area of the catalysts. SEM and EDX measurements (Figure S7 and S8, Supporting Information) were done in order to investigate the structural and compositional stability of the electrodes. After the stability tests, the electrode microstructure transformed from a more compact film to a porous structure, most likely due to the disruptive nature of evolved H_2. The EDX spectra of both MoS_2 and $MoSe_2$ electrodes exhibit peaks corresponding to C, O, F, Mo, S and Se elements. The C peak is resulted from the carbon black, Nafion and graphite electrode and whereas F and O peaks arise mainly from Nafion. The EDX spectra taken before and after the stability test shows a significant decrease in the intensity of the F and O peaks.

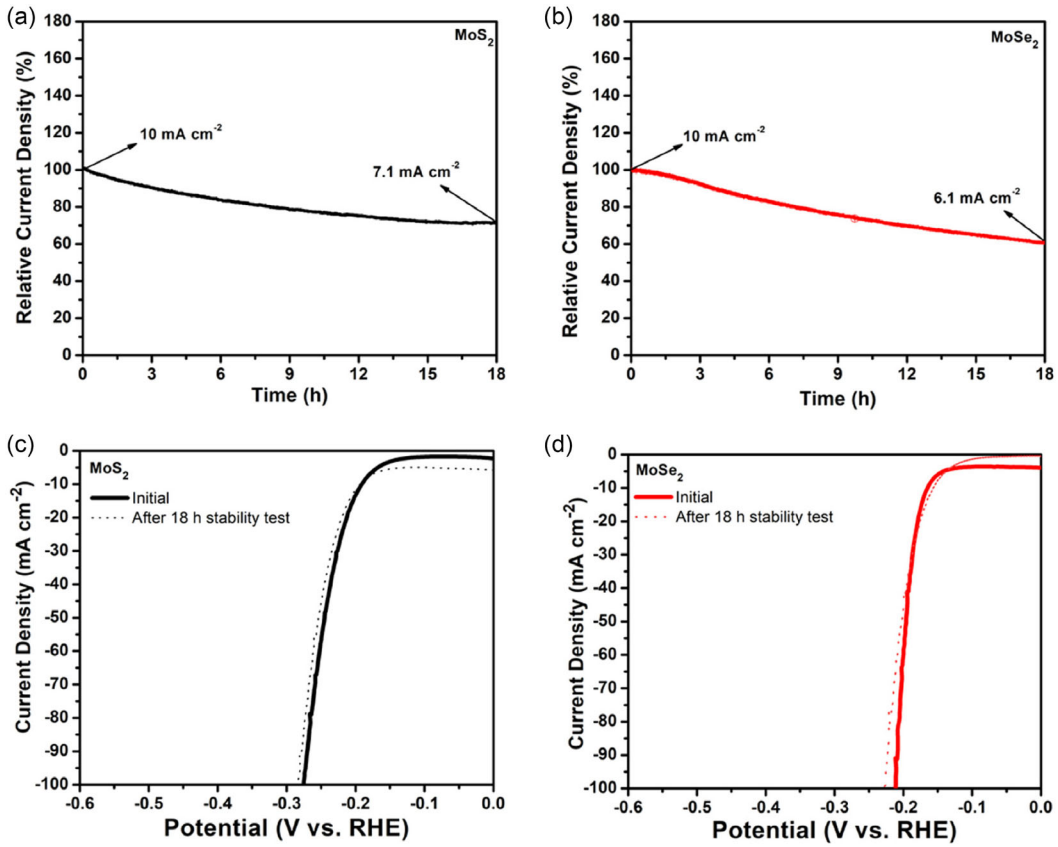

Figure 7. Chronoamperometric stability test results for the a) MoS_2 and b) $MoSe_2$ nano catalysts over a period of 18 h. LSV curves of the c) MoS_2 and d) $MoSe_2$ samples taken before and after the 18 h stability tests.

Additionally, there is a reduction in the total percentage of the elements constituting the catalysts (Mo+S and Mo+Se), which hints the partial detachment of the catalysts along with Nafion from the electrode surface. Nevertheless, both electrodes perform well in LSV measurements taken after the chronoamperometry test, which suggests that the observed morphology change in both electrodes are resulted from the physical detachment rather than chemical dissolution of the catalyst materials. Moreover, the S:Mo and Se:Mo ratio decreased after the stability test as an indication of the increased amount of sulfur and selenium vacancies, which is favorable for HER.

3. Conclusion

In summary, one-step mechanochemical synthesis of the MoS_2 and $MoSe_2$ nano catalysts has been successfully realized using planetary ball milling. This is the first demonstration of the direct mechanochemical synthesis of the MoS_2 and $MoSe_2$ nano powders. Mechanochemistry offers a facile, scalable and solvent-free approach to produce TMD nano catalysts. The effect of the synthesis parameters on the product yield was investigated. The synthesis reaction of the TMDs only took place when the BPR was increased to 100:1. The longer milling time led to higher product yield and solid dispersant at 1:1 molar ratio enhanced the yield by alleviating cold welding and agglomeration. Under the optimized conditions, the MoS_2 and $MoSe_2$ had a yield of 94.3 and 90.0%, respectively. The synthesized TMDs are in the form of nanosheets whose lateral dimensions are a few tens of nanometers and thicknesses range from 5 to 10 layers. The nanosheets mainly consist of a disordered structure in which small crystalline regions with point defects are dispersed. The surface of the nanosheets is partially oxidized and contains sulfur/selenium vacancies. The outstanding HER performance of the TMD nano catalysts could be attributed to the favorable contributions of the disordered structure, point defects and sulfur/selenium vacancies. This method provides a facile approach for the synthesis of highly disordered and catalytically active TMDs and can be readily scaled up to a production level of tens-of-gram per batch.

4. Experimental Section

Mechanochemical Synthesis of the TMD Nanosheets

Mechanochemical synthesis of the MoS_2 and $MoSe_2$ nanosheets was conducted in a laboratory scale planetary ball milling device (Fritsch, Pulverisette 5/2) using elemental Mo (Nanografi, 3 μm size, 99.95% purity), S (Merck Millipore, 99+% purity) and Se (Acros Organics, 99+% purity) powders as the precursor materials and NaCl (ISOLAB Chemicals, 99.5% purity) powder as a solid dispersant. The synthesis was carried out in a stainless steel reaction vessel (420) using 5 mm diameter stainless steel milling balls (420) with a milling speed of 400 rpm, BPR of 10:1, 50:1 and 100:1 and milling time of 24, 48 and 72 h. Prior to milling, the reaction vessel was purged with high purity Ar gas for 10 mins in order to prevent oxidation. The molar ratio of the reactants (Mo:S or Mo:Se) was kept at the stoichiometric ratio of 1:2 whereas the molar ratio of solid dispersant to the reactants (NaCl:Mo+S or NaCl:Mo+Se) was 0:1, 1:1 and 3:1. The milling process was interrupted for 10 mins after every 30 mins of operation to prevent excess heating. The resulting powder was washed with deionized water to remove NaCl and then collected using a vacuum filtration set up (0.22 μm pore size). Finally, the obtained powder was dried in an oven at 80 °C overnight and stored for characterization.

Characterization

XRD data were collected on Rigaku D-Max diffractometer equipped with a Cu-Kα source (1.54056 Å). Rietveld refinement was performed using X'Pert HighScore Plus software. TEM and EDX mapping analysis were conducted with FEI TALOS F200S electron microscope operating at 200 kV. Raman spectroscopy measurements were carried out with a WITech alpha 300 R spectrometer using a 532 nm laser excitation at 2 mW. XPS data were obtained using a SPECS FlexMod spectrometer with an Al-Kα X-ray source (1486.71 eV). The energy pass was 50 eV and the energy step was 1 eV for the survey scans whereas 20 eV energy pass and 0.1 eV energy step was used for the high-resolution scans. The binding energies were calibrated with respect to C 1s at 248.4 eV. PL spectra were recorded from 350 to 900 nm with a Dongwoo Optron spectrophotometer at room temperature using an excitation wavelength and power of 325 nm and 200 mW, respectively. BET and BJH analysis were carried out with MICROMERITICS ASAP 2020. The samples were degassed at 150 °C for 12 h prior to measurements. SEM images and EDX spectra were acquired with FEI Quanta FEG 450 scanning electron microscope.

Electrochemical Measurements

Electrochemical measurements were conducted using a Gamry Interface 1000 potentiostat in a three-electrode cell, in which the working electrode was a graphite rod, counter electrode was a Pt wire and reference electrode was a saturated calomel electrode (SCE, Als-Japan, sat. KCl). 6 mg of catalyst (MoS_2 or $MoSe_2$), 1.25 mg of carbon black (SuperP), and 35 μL of Nafion solution (5 wt%) were added to 300 μL of deionized water/isopropanol mixture (50:50 vol%) and sonicated in an ultrasonic bath for 30 mins to form a homogeneous dispersion. 20 μL of the resultant mixture was dropped onto the graphite rod electrode using a micropipette and left to dry at room temperature. The electrolyte (0.5 M H_2SO_4) was constantly stirred at 700 rpm and purged with N_2 during the measurements. LSV data were acquired with a scan rate of 5 mV s^{-1}. Potential values were converted to reversible hydrogen electrode (RHE) scale using the following equation: $E_{RHE} = E_{SCE} + E^{\circ}_{SCE} + 0.0059\,pH$, where E_{SCE} is the potential value measured with respect to the SCE reference electrode and E°_{SCE} is the standard potential of the SCE electrode at 25 °C (0.241 V). Electrochemical impedance spectroscopy (EIS) measurements were performed at an overpotential of 0.25 V by applying an AC perturbation of 10 mV within the frequency range of 0.1 Hz to 1 MHz. Chronoamperometry measurements were carried out at 10 mA cm^{-2} current density for 18 h to assess the stability of the catalysts. To obtain double layer capacitance (C_{dl}), cyclic voltammetry (CV) scans were recorded in the potential range of 0.1–0.3 V versus RHE at different scan rates (20, 40, 60, 80 and 100 mV s^{-1}). After each measurement, the surface of the graphite rod electrode was manually polished with alumina slurry and cleaned in an ultrasonic bath in deionized water/isopropanol mixture.

Acknowledgements

This work was funded by The Scientific Research Projects Unit of Bilecik Seyh Edebali University (BAP) (Grant No. 2023-01.BŞEÜ.03-12).

Conflict of Interest

The authors declare no conflict of interest.

Data Availability Statement

The data that support the findings of this study are available from the corresponding author upon reasonable request.

Keywords: heterogeneous catalysts · hydrogen evolution reaction · mechanochemical synthesis · nanotechnology · transition metal dichalcogenides

[1] R. U. Ayres, J. Walter, *Environ. Resour. Econ.* **1991**, *1*, 237.
[2] K. Bäckstrand, *Palgrave. Macmillan. Cham.* **2022**, 39-61.
[3] K. Mazloomi, C. Gomes, *Renew. Sust. Energ.* **2012**, *16*, 3024.
[4] Y. Pan, Y. Zhu, *J. Alloys Compd.* **2025**, *1021*, 179661.
[5] Y. Pan, J. Gao, *J. Energy Storage* **2025**, *124*, 116869.
[6] Y. Pan, Y. Zhu, *Int. J. Hydrogen Energy* **2025**, *131*, 221.
[7] J. Gao, Y. Pan, I. P. Jain, F. Yang, J. Zhu, *Appl. Mater. Today* **2025**, *44*, 102755.
[8] Y. Zhu, Y. Pan, F. Yang, J. Zhu, *Int. J. Hydrogen Energy* **2025**, *136*, 11.
[9] F. Yang, Y. Pan, J. Zhu, *Appl. Surf. Sci.* **2025**, *680*, 161321.
[10] B. S. Zainal, P. J. Ker, H. Mohamed, H. C. Ong, I. M. R. Fattah, S. A. Rahman, T. I. Mahlia, *Renew. Sustain. Energy Rev.* **2024**, *189*, 113941.
[11] I. Dincer, *Int. J. Hydrogen Energy* **2012**, *37*, 1954.
[12] Q. Hassan, A. M. Abdulateef, S. A. Hafedh, A. Al-samari, J. Abdulateef, A. Z. Sameen, H. M. Salman, A. K. Al-Jiboory, S. Wieteska, M. Jaszczur, *Int. J. Hydrogen Energy* **2023**, *29*, 17383.
[13] J. Merwe, K. Uren, G. Schoor, D. Bessarabov, *Int. J. Hydrogen Energy* **2014**, *39*, 14212.
[14] Z. Wang, S. Liu, W. Duan, Y. Xing, Y. Hu, Y. Ma, *Int. J. Hydrogen Energy* **2024**, *22*, 1414.
[15] E. Kemppainen, A. Bodin, B. Sebok, T. Pedersen, B. Seger, B. Mei, D. Bae, P. C. K. Vesborg, J. Halme, O. Hansen, P.D. Lund, *Energy Environ. Sci.* **2015**, *8*, 2991.
[16] Y. Zheng, Y. Jiao, M. Jaroniec, S. Z. Qiao, *Angew. Chem. Int. Edn.* **2014**, *54*, 52.
[17] S. Bai, C. Wang, M. Deng, M. Gong, Y. Bai, J. Jiang, Y. Xiong, *Angew. Chem. Int. Edn.* **2014**, *53*, 12120.
[18] Q. Lu, Y. Yu, Q. Ma, *Adv. Mater.* **2015**, *28*, 1917.
[19] F. Wang, T. A. Shifa, X. Zhan, Y. Huang, K. Liu, Z. Cheng, C. Jiang, J. He, *Nanoscale* **2015**, *7*, 19764.
[20] X. Chia, A. Y. S. Eng, A. Ambrosi, S. M. Tan, M. Pumera, *Chem. Rev.* **2015**, *115*, 11941.
[21] T. F. Jaramillo, K. P. Jorgensen, J. Bonde, J. H. Nielsen, S. Horch, I. Chorkendorff, *Science* **2007**, *317*, 100.
[22] C. Tsai, K. Chan, J. K. Nørskov, F. Abild-Pedersen, *Surf. Sci.* **2015**, *640*, 133.
[23] J. Kibsgaard, Z. Chen, B. N. Reinecke, T. F. Jaramillo, *Nat. Mater.* **2012**, *11*, 963.
[24] H. Wang, Z. Lu, D. Kong, J. Sun, T. M. Hymel, Y. Cui, *ACS Nano* **2014**, *8*, 4940.
[25] J. Shi, D. Ma, G. F. Han, Y. Zhang, Q. Ji, T. Gao, J. Sun, X. Song, C. Li, Y. Zhang, X. Y. Lang, *ACS Nano* **2014**, *8*, 10196.
[26] F. H. Saadi, A. I. Carim, J. M. Velazquez, J. H. Baricuatro, C. C. McCrory, M. P. Soriaga, N.S. Lewis, *ACS Catal.* **2014**, *4*, 2866.
[27] G. D. Park, J. H. Kim, S. K. Park, Y. C. Kang, *ACS Appl. Mater. Interfaces* **2017**, *9*, 10673.
[28] Y. Li, H. Wang, L. Xie, *J. Am. Chem. Soc.* **2011**, *133*, 7296.
[29] Z. Chen, D. Cummins, B. N. Reinecke, E. Clark, M. K. Sunkara, T. F. Jaramillo, *Nano Lett.* **2011**, *11*, 4168.
[30] C. Wang, P. Zhang, J. Lei, *Electrochim. Acta* **2017**, *246*, 712.
[31] Y. Qu, H. Medina, S. W. Wang, *Adv. Mater.* **2016**, *28*, 9831.
[32] J. D. Yi, T. T. Liu, Y. B. Huang, R. Cao, *Sci. China Mater.* **2019**, *62*, 965.
[33] X. Chia, M. Pumera, *ACS Appl. Mater. Interfaces* **2018**, *10*, 4937.
[34] B. Mohanty, A. Mitra, B. Jena, B. K. Jena, *Energy Fuels* **2020**, *34*, 10268.
[35] Y. Yin, Y. Zhang, T. Gao, *Adv. Mater.* **2017**, *29*, 1700311.
[36] Y. Zhao, X. Xie, J. Zhang, *Chem. Eur. J.* **2015**, *21*, 15908.
[37] S. K. Behera, P. Deb, A. Ghosh, *ChemistrySelect* **2017**, *2*, 3657.
[38] C. Tsai, H. Li, S. Park, J. Park, H. S. Han, J. K. Nørskov, X. Zheng, F. Abild-Pedersen, *Nat. Commun.* **2017**, *8*, 15113.
[39] K. Wu, C. Wang, X. Lang, J. Cheng, H. Wu, C. Lyu, W. M. Lau, Z. Liang, X. Zhu, J. Zheng, *J. Colloid. Sci.* **2024**, *15*, 1040.
[40] D. Merki, S. Fierro, H. Vrubel, X. Hu, *Chem. Sci.* **2011**, *2*, 1262.
[41] Q. T. Nguyen, P.D. Nguyen, D. Nguyen, Q. D. Truong, T. T. Kim-Chi, T. T. D. Ung, I. Honma, N. Q. Liem, P. D. Tran, *ACS Appl. Mater. Interfaces* **2018**, *10*, 8659.
[42] J. You, M. D. Hossain, Z. Luo, *Nano Converg.* **2018**, *5*, 1.
[43] F. R. Chen, *Chem. Mater.* **2001**, *13*, 802.
[44] C. Tan, H. Zhang, *Nat. Commun.* **2015**, *6*, 1.
[45] J. N. Coleman, M. Lotya, A. O'Neill, S. D. Bergin, P. J. King, U. Khan, K. Young, A. Gaucher, S. De, R. J. Smith, I. V. Shvets, *Science* **2011**, *331*, 568.
[46] Q. Zhang, L. Mei, X. Cao, Y. Tang, Z. Zeng, *J. Mater. Chem. A* **2020**, *8*, 15417.
[47] N. Liu, P. Kim, J. H. Kim, J. H. Ye, S. Kim, C. J. Lee, *ACS Nano* **2014**, *8*, 6902.
[48] T. Tsuzuki, P. G. McCormick, *J. Mater. Sci.* **2004**, *39*, 5143.
[49] C. Xu, S. De, A. M. Balu, *ChemComm.* **2015**, *51*, 6698.
[50] T. Tsuzuki, P. G. McCormick, *Nanostructured Mater.* **1999**, *12*, 75.
[51] Z. Wu, D. Wang, A. Sun, *J. Alloys Compd.* **2010**, *492*, L5.
[52] O. Y. Posudievsky, O. A. Kozarenko, V. S. Dyadyun, *Electrocatalysis* **2019**, *10*, 477.
[53] B. Hu, Y. Wu, K. Wang, H. Guo, Z. Lei, Z. Liu, L. Wang, *Small* **2024**, *20*, 2305344.
[54] G. Deokar, D. Vignaud, R. Arenal, P. Louette, J. F. Colomer, *Nanotechnology* **2016**, *27*, 075604.
[55] M. H. Wu, J. T. Lee, Y. J. Chung, *Nano Energy* **2017**, *40*, 369.
[56] D. Vikraman, K. Akbar, S. Hussain, *Nano Energy* **2017**, *35*, 101.
[57] S. Hussain, S. A. Patil, D. Vikraman, *J. Electrochem. Soc.* **2017**, *164*, E11.
[58] S. Acharya, S. Mansingh, K. M. Parid, *Inorg. Chem. Front.* **2017**, *4*, 1022.
[59] L. Gago-Duport, M. J. I. Briones, J. B. Rodríguez, B. Covelo, *J. Struct. Biol.* **2008**, *162*, 422.
[60] L. Li, Z. Qin, L. Ries, S. Hong, T. Michel, J. Yang, C. Salameh, M. Bechelany, P. Miele, D. Kaplan, M. Chhowalla, *ACS Nano* **2019**, *13*, 6824.
[61] M. Song, H. Tan, X. Li, A. I. Y. Tok, P. Liang, D. Chao, H. J. Fan, *Small Methods* **2020**, *12*, 1900274.
[62] X. Huang, M. Leng, W. Xiao, M. Li, J. Ding, T. L. Tan, W. S. V. Lee, J. Xue, *Adv. Funct. Mater.* **2016**, *27*, 1604943.
[63] X. Xiao, S. Shen, L. Zhang, Z. Lin, Z. Wang, Q. Zhang, W. Zhong, B. Zhan, *Chem. Asian J.* **2023**, *18*, 1.
[64] S. J. Patil, N. R. Chodankar, S. K. Hwang, P. A. Shinde, G. S. R. Raju, K. S. Ranjith, Y. S. Huh, Y. K. Han, *J. Chem. Eng.* **2022**, *429*, 132379.
[65] R. Szoszkiewicz, *Mater.* **2021**, *14*, 5979.
[66] H. Li, Q. Zhang, C. C. R. Yap, *Adv. Func. Mater.* **2012**, *22*, 1385.
[67] D. Nam, J. U. Lee, H. Cheong, *Sci. Rep.* **2015**, *5*, 17113.
[68] E. Schut, R. M. Breedijk, M. F. Hilbers, M. A. Hink, T. Krap, M. C. Aalders, R. M. Williams, *Photochem. Photobiol. Sci.* **2024**, *23*, 1641.
[69] T. Shinagawa, A. T. Garcia-Esparza, K. Takanabe, *Sci. Rep.* **2015**, *5*, 13801.
[70] Z. Wang, Q. Li, H. Xu, *Nano Energy* **2018**, *49*, 634.
[71] Y. Wang, B. J. Carey, W. Zhang, *J. Phys. Chem. C* **2016**, *120*, 2447.
[72] G. Gao, A. P. O'Mullane, A. Du, *ACS Catal.* **2016**, *7*, 494.
[73] Q. Fu, J. Han, X. Wang, *Adv. Mater.* **2020**, *33*, 1907818.
[74] L. Wu, A. Longo, N. Y. Dzade, A. Sharma, M. M. Hendrix, A. A. Bol, N. H. De-Leeuw, E. J. Hensen, J. P. Hofmann, *ChemSusChem* **2019**, *12*, 4383.
[75] Y. Li, K. Yin, L. Wang, X. Lu, Y. Zhang, Y. Liu, D. Yan, Y. Song, S. Luo, *Appl. Catal. B: Environ.* **2018**, *239*, 537.
[76] Y. Cheng, H. Song, H. Wu, P. Zhang, Z. Tang, S. Lu, *Chem. Asian J.* **2020**, *15*, 3123.
[77] X. Wang, Y. Zhang, H. Si, Q. Zhang, J. Wu, L. Gao, X. Wei, Y. Sun, Q. Liao, Z. Zhang, K. Ammarah, *J. Am. Chem. Soc.* **2020**, *142*, 4298.
[78] S. Anantharaj, S. Noda, M. Driess, P. W. Menezes, *ACS Energy Lett.* **2021**, *6*, 1607.
[79] B. Qu, X. Yu, Y. Chen, *ACS Appl. Mater. Interfaces* **2015**, *7*, 14170.
[80] S. Shin, Z. Jin, D. H. Kwon, *Langmuir* **2015**, *31*, 1196.
[81] R. Jin, S. Su, J. Li, D. Ping, Y. Li, M. He, X. Yu, Z. Wei, Y. Liu, S. Li, J. Zheng, *Nanomaterials* **2024**, *14*, 1422.
[82] B.K. Barman, D. Das, K.K. Nanda, *J. Mater. Chem. A* **2017**, *5*, 18081.
[83] C. Sun, J. Zhang, J. Ma, P. Liu, D. Gao, K. Tao, D. Xue, *J. Mater. Chem. A* **2016**, *4*, 11234.
[84] D. R. Paudel, U. N. Pan, R. B. Ghising, P. P. Dhakal, V. A. Dinh, H. Wang, N. H. Kim, J.H. Lee, *Nano Energy* **2022**, *102*, 107712.
[85] Y. Jing, X. Mu, C. Xie, H. Liu, R. Yan, H. Dai, C. Liu, X. D. Zhang, *Int. J. Hydrogen Energy* **2019**, *44*, 809.
[86] J. Paštika, D. Güngen, A. Subramani, V. Mazánek, M. Serra, L. Zeng, E. Olsson, R. Gusmão, Z. Ssofer, *ACS Appl. Mater. Interfaces* **2025**, *17*, 3552235532.

[87] K. S. Bhat, H. S. Nagaraja, *Int. J. Hydrogen Energy* **2019**, *44*, 17878886.
[88] M. A. Worsley, S. J. Shin, M. D. Merrill, J. Lenhardt, A. J. Nelson, L. Y. Woo, A. E. Gash, T. F. Baumann, C. A. Orme, *ACS Nano* **2015**, *9*, 4698.
[89] S. H. Yu, Z. Tang, Y. Shao, H. Dai, H.Y. Wang, J. Yan, H. Pan, D. H. Chua, *ACS Appl. Energy Mater.* **2019**, *2*, 5799.
[90] M. Li, B. Cai, R. Tian, X. Yu, M. B. Breese, X. Chu, Z. Han, S. Li, R. Joshi, A. Vinu, T. Wan, *Chem. Eng. J.* **2021**, *409*, 128158.
[91] S. Xie, B. Sun, H. Sun, K. Zhan, B. Zhao, Y. Yan, B. Y. Xia, *Int. J. Hydrogen Energy* **2019**, *44*, 15009.
[92] H. An, W. Park, H. Shin, D. Y. Chung, *EcoMat* **2024**, *6*, 1.
[93] J. Xie, J. Zhang, S. Li, F. Grote, X. Zhang, H. Zhang, Y. Xie, *J. Am. Chem. Soc.* **2013**, *135*, 17881.
[94] C. Zhang, L. Jiang, Y. Zhang, J. Hu, M. K. Leung, *J. Catal.* **2018**, *361*, 384.

Manuscript received: May 5, 2025
Revised manuscript received: June 22, 2025
Version of record online: